

Direct Measurement of 2D and 3D Interprecipitate Distance Distributions from Atom-Probe Tomographic Reconstructions

Richard A. Karnesky,* Dieter Isheim, and David N. Seidman

Department of Materials Science and Engineering and the Northwestern

University Center for Atom-Probe Tomography (NUCAPT)

Evanston, IL 60208-3108, USA[†]

(Dated: 2007-04-30)

Abstract

Edge-to-edge interprecipitate distance distributions are critical for predicting precipitation strengthening of alloys and other physical phenomena. A method to calculate this 3D distance and the 2D interplanar distance from atom-probe tomographic data is presented. It is applied to nanometer-sized Cu-rich precipitates in an Fe-1.7 at.% Cu alloy. Experimental interprecipitate distance distributions are discussed.

*Electronic address: karnesky@northwestern.edu

[†]URL: <http://arc.nucapt.northwestern.edu/>

Many physical properties of materials depend on the edge-to-edge interprecipitate distance, λ_{e-e} . The applied stress required for a dislocation to glide past or climb over precipitates depends on λ_{e-e} [1], as does precipitate coarsening and electrical conductivity. Frequently, λ_{e-e} is merely approximated by assuming the precipitates form a cubic array or a square array in a plane [2]. It is also assumed that precipitates are spherical with a known precipitate size distribution (PSD) (usually either all precipitates are the same size or they obey the PSD derived by Lifshitz and Slyozov [3] and Wagner [4] (LSW)). Real materials are almost always more complicated.

Much of the past work on calculating the distance between precipitates or other microstructural features of interest [5, 6] (whether interprecipitate distances [2], mean free paths or chord lengths [7], or nearest-neighbor distribution functions [8, 9, 10, 11]) has been theoretical. Experimental characterization of λ_{e-e} requires a microscopic technique that has: (i) a high enough spatial resolution to define clearly each and every precipitate; (ii) a large enough analysis volume to capture many precipitates and to exclude boundary effects; and (iii) 3-dimensional information (without suffering from precipitate overlap or truncation). For nanometer-sized precipitates, the local-electrode atom-probe (LEAP[®]) tomograph (Imago Scientific Instruments) satisfies these requirements [12, 13]. Despite these capabilities, it has not been previously utilized to gather this information and the little available experimental data for λ_{e-e} comes from 2D techniques. These cannot be compared directly to models of 3D microstructure, but only to 2D slices from theoretical 3D microstructures [14].

In this article, an algorithm to calculate λ_{e-e} from LEAP tomographic reconstructions is presented and applied to a binary Fe-Cu alloy. This alloy and many other steels are strengthened by a high number density of nanometer-sized copper-rich precipitates [15]. Many of the proposed precipitate strengthening mechanisms depend on λ_{e-e} [16, 17]. Atom-probe tomography has been used to study the size, morphology, and chemical composition of Cu precipitates [18, 19, 20, 21, 22], but not to measure λ_{e-e} . An Fe-1.7 at.% Cu alloy was solutionized at 1000°C for 1 h and 845°C for 6 h. It was subsequently aged for 2 h at 500°C. This treatment leads to a high number density ($(1.2 \pm 0.1) \times 10^{24} \text{ m}^{-3}$) of nanometer-sized precipitates (with a mean radius, $\langle R \rangle$, equal to 1.3 nm). The specimens were cut, ground, and then electropolished into tips. The LEAP tomographic experiment was conducted with a 50 K specimen temperature, a 5–10 kV specimen voltage, pulse fraction of 15%, and a

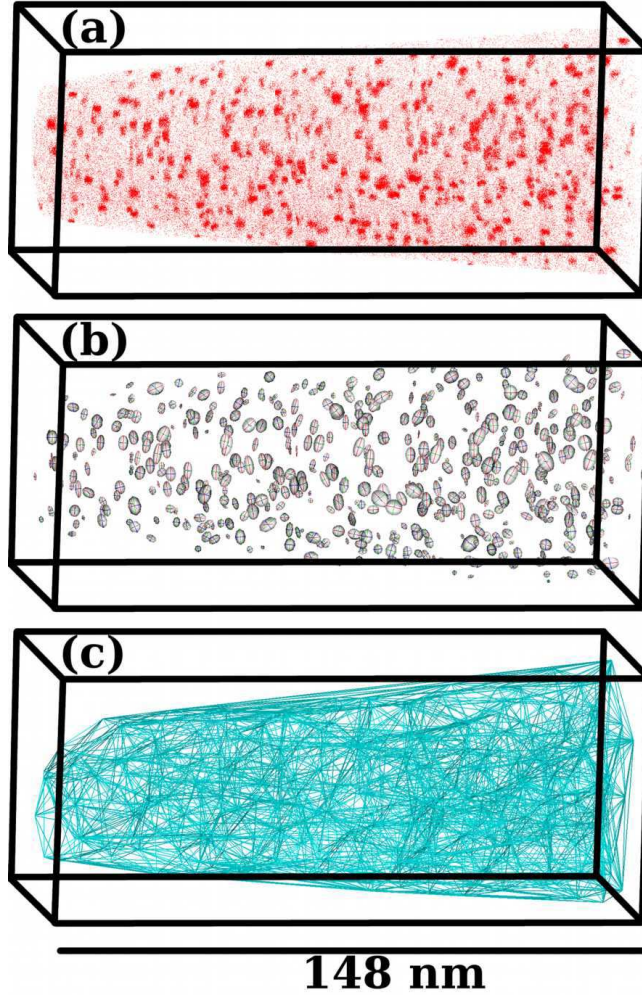


FIG. 1: (a) A LEAP[®] tomographic reconstruction of an Fe-1.7 at.% Cu specimen, whose thermal history is detailed in the text. Only Cu atoms are displayed for clarity. (b) The 546 precipitates are fitted as ellipsoids [23] (c) A Delaunay mesh connects the precipitate centers. This is used to find “interacting precipitates” and to exclude the convex hull.

pulse repetition rate of 200 kHz to collect ca. 1.3×10^6 ions in a $148 \times 66 \times 62 \text{ nm}^3$ volume (Fig. 1a). The computer program IVAS (Imago Scientific Instruments) was used to analyze the data. Precipitates are isolated using a modified envelope algorithm [24]. Because Cu partitions strongly to precipitates [21], an isoconcentration surface was not necessary to distinguish the 546 precipitates in this dataset.

The interprecipitate distance algorithm begins by representing these precipitates with simpler geometric shapes. While λ_{e-e} between spheres is simple (it being the difference of

the center-to-center distance and the precipitate radii), spheres do not adequately represent many precipitate morphologies. Instead, best-fit ellipsoids to the precipitates are calculated (Fig. 1b) employing a recently presented algorithm [23]. The 4×4 transformation matrix calculated with that algorithm translates, rotates, and scales a unit sphere centered at the origin to an ellipsoid that preserves the centroid, principle axes, and moments of inertia of a precipitate.

A Delaunay tetrahedral mesh is generated from the precipitate centroids (Fig. 1c) [25, 26]. The Delaunay mesh is the geometric dual of the Voronoi diagram; mesh segments connect neighboring precipitates whose Voronoi cells touch. It decreases the number of precipitate pairs for which λ_{e-e} is calculated to a group of neighbors. The mesh also finds the 75 precipitates that make up the convex hull. These outer-most precipitates are allowed to be nearest neighbors of the inner precipitates, but their own nearest neighbors are not calculated, as they might fall outside the volume of the analysis.

The distance between two ellipsoids is found utilizing the constrained optimization by linear approximation (COBYLA) algorithm [27]. This general optimization algorithm is chosen over more efficient algorithms that calculate explicitly the distance between ellipsoids [28, 29], so that it can be used with other abstractions of precipitate morphology (such as the isoconcentration surface) and additional constraints (such as calculation of interplanar edge-to-edge distances) and because a gratis implementation exists [30]. COBYLA minimizes the distance between two points, x and y in the analysis space, $\sqrt{\sum_j (x_j - y_j)^2}$. The constraints are that x and y must fall on the ellipsoid. This is simplified by the fact that applying the inverse transformation of ellipsoids transforms them back into unit spheres, centered at the origin (so $\sum_j x_j^{T_x} = 1$ and $\sum_j y_j^{T_y} = 1$, where the superscript T_i is the inverse transform of the best-fit ellipsoid for precipitate i). The initial guess is chosen as the two closest points that satisfy these constraints that lie on the line that connects the precipitate centers. Interprecipitate distance distributions (IDDs) may be generated using different combinations of Delaunay neighbors, as in Fig. 2. An IDD is the convolution of a PSD and the center-to-center distances. In Fig. 2a, an IDD for all 6,671 Delaunay neighbor distances yields a mean 3D interprecipitate distance, $\langle \lambda_{e-e}^{3D} \rangle$, of 16 nm. Figure 2b displays two subsets of this IDD, each with 471 lengths. The distance between nearest precipitates is often used to calculate precipitate-dislocation interactions. The IDD for this is much sharper and $\langle \lambda_{e-e}^{3D} \rangle = 2.6$ nm. Precipitates that are very close to one another might be bypassed as

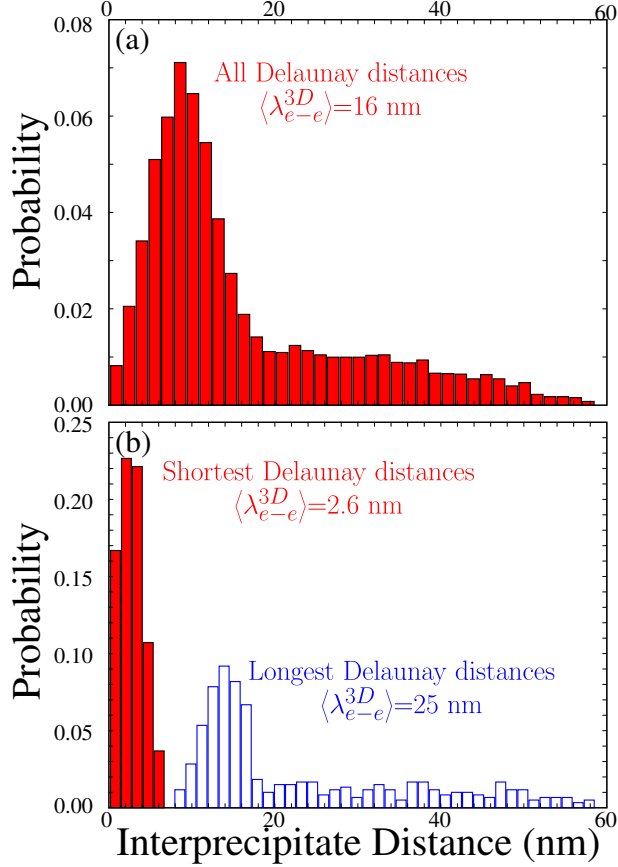


FIG. 2: 3D IDD for the dataset in Fig. 1. (a) IDD of all 6,771 Delaunay lengths, with $\langle \lambda_{e-e}^{3D} \rangle = 16$ nm. (b) Solid: IDD of nearest-neighbor distances, which is much sharper than when longer lengths are included ($\langle \lambda_{e-e}^{3D} \rangle = 2.6$ nm). Hollow: IDD of the most-distant Delaunay neighbors, which is broader than and does not overlap with the shortest distances ($\langle \lambda_{e-e}^{3D} \rangle = 25$ nm).

a pair by a dislocation. The longest Delaunay distances provide an upper bound to the interactive distance. This is probably not physically important for plastic deformation, but may be relevant for other physical phenomena. The IDD for this case is broader, does not overlap the shortest distances, and has a mean value that is an order of magnitude larger ($\langle \lambda_{e-e}^{3D} \rangle = 25$ nm).

In certain cases, it is not $\langle \lambda_{e-e}^{3D} \rangle$ that is of interest, but rather the interplanar edge-to-edge distance, $\langle \lambda_{e-e}^{2D} \rangle$. This might, for instance, be a glide plane of a dislocation. This 2D distance can be calculated by imposing an additional constraint for COBYLA—that x and y values must fall on a particular plane. For comparison, $\langle \lambda_{e-e}^{3D} \rangle$ and $\langle \lambda_{e-e}^{2D} \rangle$ can be calculated

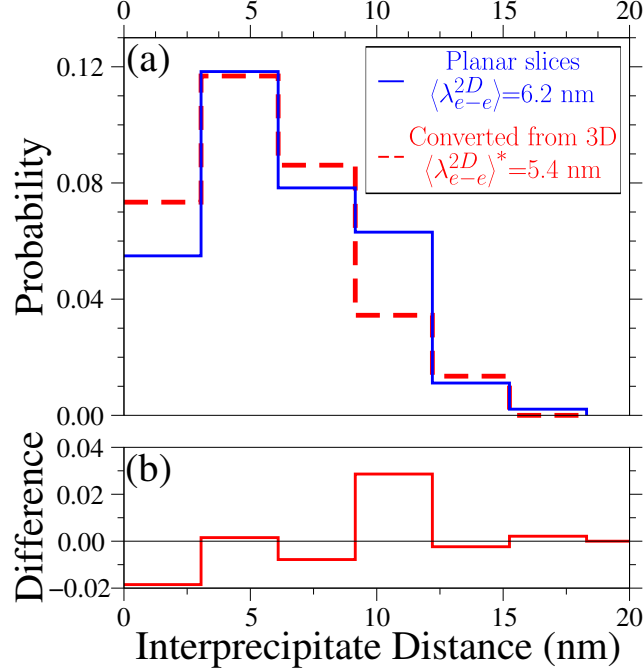


FIG. 3: (a) Interplanar (2D) IDD for the dataset in Fig. 1. Solid: IDD of slices, with $\langle \lambda_{e-e}^{2D} \rangle = 6.2 \text{ nm}$. Dashed: IDD from Fig. 2b scaled by Eq. 3 ($\langle \lambda_{e-e}^{2D} \rangle^* = 5.4 \text{ nm}$). (b) λ_{e-e}^{2D} is weighted towards longer distances than λ_{e-e}^{2D*}

from one another by assuming precipitates are distributed on a cubic lattice [2],

$$\langle \lambda_{e-e}^{3D} \rangle = \left(\sqrt[3]{\frac{4\pi}{3\phi}} - 2 \right) \langle R \rangle; \quad (1)$$

where ϕ is the volume fraction of precipitates. Assuming a square array of precipitates,

$$\langle \lambda_{e-e}^{2D} \rangle = \left(\sqrt{\frac{\pi}{\phi}} - 2 \right) \bar{R}; \quad (2)$$

where the mean planar radius, \bar{R} , is equal to $\frac{\pi}{4}\omega_2\langle R \rangle$, with ω_2 dependent on the PSD [2]. Values for ω_2 for the LSW distribution and for the case where all precipitates are the same size are given in Ref. [2]. Equating the ϕ s in Eqs. 1–2 leads to a cubic equation relating $\langle \lambda_{e-e}^{2D} \rangle$ and $\langle \lambda_{e-e}^{3D} \rangle$. Solving for $\langle \lambda_{e-e}^{2D} \rangle$:

$$\langle \lambda_{e-e}^{2D} \rangle = \frac{\pi \left(-4\omega_2\langle R \rangle^2 + \sqrt{3\omega_2^2\langle R \rangle (2\langle R \rangle + \langle \lambda_{e-e}^{3D} \rangle)^3} \right)}{8\langle R \rangle}. \quad (3)$$

In Fig. 3, the results of the two methods for extracting 2D nearest-neighbor IDD from the

3D dataset are compared. λ_{e-e}^{2D} is calculated directly by imposing the additional constraint on COBYLA that the two points must lie in the same plane, which is radial to the analysis direction. The entire tip is sampled by taking 180 1° steps. This process samples the precipitates toward the center of the tip more than those toward the hull, but has fewer edge artifacts than parallel slices would have. λ_{e-e}^{2D*} is calculated from what is displayed in Fig. 2b by applying Eq. 3 with $\langle R \rangle = 1.3$ nm and $\omega_2 = 1.046$ [2] (the superscript * denotes this transformation). Despite the simple geometrical assumptions involved in deriving Eq. 3, the mean values are in reasonable agreement (with the “direct” method yielding $\langle \lambda_{e-e}^{2D} \rangle = 6.2$ nm and with the conversion leading to $\langle \lambda_{e-e}^{2D} \rangle^* = 5.4$ nm). Despite this similarity in the mean values, the distributions are different. The converted IDD is narrower and weighted towards shorter distances than the IDD that is directly calculated.

This supports the conclusion reached in Ref. [14], that λ_{e-e} should be calculated directly with the same dimensionality as either the simulations they are compared with or the physical models they are be used in. 2D techniques can *only* result in 2D IDD, and will not yield accurate 3D IDD. They may give a reasonable estimate of $\langle \lambda_{e-e}^{3D} \rangle$, although 3D experimental data, as is gathered with the LEAP tomograph, allows both λ_{e-e}^{3D} to be measured and λ_{e-e}^{2D} to be measured from planar slices taken from the 3D reconstruction.

We are in the midst of applying this approach to calculate the strength of different alloys using analytical equations [2]. We are also using it to evaluate the statistical accuracy of simulated microstructures, which are used in a continuum dislocation dynamics simulation that calculates a stress-strain curve [31].

Acknowledgments

This research is supported by the Office of Naval Research, under contract N00014-03-1-0252. RAK received partial support from a Walter P. Murphy Fellowship and the US Department of Energy (DE-FG02-98ER45721). We thank Dr. S. K. Lahiri and Prof. M. E. Fine for providing the Fe-Cu alloy. Imago Scientific Instruments and Dr. M. K. Miller permitted RAK to modify the source code for ENVELOPE. Profs. D. C. Dunand and J.

Jerome are thanked for discussions.

- [1] L. M. Brown and R. K. Ham, in *Strengthening Mechanisms in Crystals*, edited by A. Kelly and R. B. Nicholson (Applied Science, London, 1971), pp. 9–135.
- [2] E. Nembach, *Particle Strengthening of Metals and Alloys* (Wiley-Interscience, New York, 1996).
- [3] I. M. Lifshitz and V. V. Slyozov, *J. Phys. Chem. Solids* **19**, 35 (1961).
- [4] C. Wagner, *Z. Electrochem.* **65**, 581 (1961).
- [5] S. Torquato, *Annu. Rev. Mater. Res.* **32**, 77 (2002).
- [6] J. Quintanilla, *Polym. Eng. Sci.* **39**, 559 (2004).
- [7] B. Lu and S. Torquato, *J. Chem. Phys.* **98**, 6472 (1993).
- [8] S. Torquato, *Phys. Rev. E* **51**, 3170 (1995).
- [9] J. R. Macdonald, *J. Phys. Chem.* **96**, 3861 (1996).
- [10] Z. H. Liu, Y. Li, and K. W. Kowk, *Polymer* **42**, 2701 (2001).
- [11] A. Tewari and A. M. Gokhale, *Mater. Sci. Eng. A* **385**, 332 (2004).
- [12] T. F. Kelly and D. J. Larson, *Mater. Char.* **44**, 59 (2000).
- [13] D. N. Seidman, *Annu. Rev. Mater. Res.* **37**, 127 (2007).
- [14] J. W. Leggoe, *Scr. Mater.* **53**, 1263 (2005).
- [15] S. K. Lahiri and M. E. Fine, *Metall. Trans.* **1**, 1495 (1970).
- [16] M. E. Fine and D. Isheim, *Scr. Mater.* **53**, 115 (2005).
- [17] J. Liu, A. van de Walle, G. Ghosh, and M. Asta, *Phys. Rev. B* **72**, 144109:1 (2005).
- [18] S. R. Goodman, S. S. Brenner, and J. R. Low, *Metall. Trans.* **4**, 2363 (1973).
- [19] M. K. Miller, K. F. Russell, P. Pareige, M. J. Starink, and R. C. Thomson, *Mater. Sci. Eng. A* **250**, 49 (1998).
- [20] M. Murayama, Y. Katayama, and K. Hono, *Metall. Mater. Trans. A* **30**, 345 (1999).
- [21] D. Isheim, M. S. Gagliano, M. E. Fine, and D. N. Seidman, *Acta Mater.* **54**, 841 (2006).
- [22] D. Isheim, R. P. Kolli, M. E. Fine, and D. N. Seidman, *Scr. Mater.* **55**, 35 (2006).
- [23] R. A. Karnesky, C. K. Sudbrack, and D. N. Seidman, *Scr. Mater.* **Accepted April 2007** (2007).
- [24] M. K. Miller and E. A. Kenik, *Microsc. Microanal.* **10**, 336 (2004).

- [25] K. Clarkson, in *Proc. 31st IEEE Symposium on Foundations of Computer Science* (Pittsburgh, PA, 1992), pp. 387–395.
- [26] C. B. Barber, D. P. Dobkin, and H. Huhdanpaa, *ACM Transactions on Mathematical Software* **22**, 469 (1996).
- [27] M. Powell, in *Advances in Optimization and Numerical Analysis*, edited by S. Gomez and J. Hennart (Kluwer Academic, Dordrecht, 1994), pp. 51–67.
- [28] A. Lin and S.-P. Han, *SIAM J. Optimization* **13**, 298 (2002).
- [29] K.-A. Sohn, B. Jüttler, M.-S. Kim, and W. Wang, in *PG 2002*, edited by S. Coquillart, H.-Y. Shum, and S.-M. Shi-Min Hu (IEEE Computer Society, 2002), pp. 236–245.
- [30] E. Jones, T. Oliphant, P. Peterson, et al., *SciPy: Open source scientific tools for Python* (2001–).
- [31] V. Mohles, *Mater. Sci. Eng. A* **365**, 144 (2004).